aerospace

MDPI

Article

Stability Enhancement and Noise Reduction of an Axial Compressor with Foam Metal Casing Treatment

Jia Li [1], Xu Dong [2], Dakun Sun [1,3,*], Yuqing Wang [1], Chunwang Geng [1] and Xiaofeng Sun [1,2]

[1] School of Energy and Power Engineering, Beihang University, Beijing 100191, China
[2] Research Institute of Aero-Engine, Beihang University, Beijing 100191, China
[3] National Key Laboratory of Science and Technology on Aero-Engine Aero-Thermaldynamics, Beihang University, Beijing 100191, China
* Correspondence: sundk@buaa.edu.cn

Abstract: Foam metal is a foam-like substance with a high porosity; it has been used in flow control, vibration abatement, and acoustic absorption, mainly based on its physical properties. The aim of the current paper is to investigate the effect of foam metal casing treatments on the stability and acoustic level of a low-speed axial flow compressor. The experimental results show that the casing treatment improves the stall margin by 14.9%, without any efficiency loss. In terms of noise, the *SPL* of the tonal noise at the third order of BPF is reduced by 3.2 dB, while the *SPL* of the broadband noise is reduced up to 2.4 dB. The comparison in evolutions of the tip structure in a smooth casing condition and with a casing treatment indicates that the casing treatment affects the origination and the development of the tip leakage vortex. The working mechanism is also discussed.

Keywords: rotating stall; casing treatment; compressor; noise; stall margin

Citation: Li, J.; Dong, X.; Sun, D.; Wang, Y.; Geng, C.; Sun, X. Stability Enhancement and Noise Reduction of an Axial Compressor with Foam Metal Casing Treatment. *Aerospace* **2022**, *9*, 628. https://doi.org/10.3390/aerospace9100628

Academic Editor: Konstantinos Kontis

Received: 31 August 2022
Accepted: 18 October 2022
Published: 21 October 2022

1. Introduction

It has been recognized for more than fifty years that the casing treatments are effective in improving the stall margin and distortion tolerance of a compressor [1]. The casing treatments were first investigated experimentally at NASA, and subsequently, a great deal of effort has been put into researching this subject. [2].

The development of casing treatments has gone through three different stages. At first, attention was focused on finding casing treatment configurations that could enhance the compressor stability. Many configurations, including perforated, groove-type, slot-type, and honeycombs casing, have been tried [1,3–5]. It has been determined that the slot-type casing treatment generally generates a significant stall margin, but usually causes a large efficiency loss. The groove-type casing treatments cause smaller efficiency loss, as well as a smaller stall margin. The common conclusion drawn, based on these results, is that stall margin improvement always occurs along with efficiency loss [6]. Therefore, the inner working mechanism regarding casing treatments has received a great deal of attention for decades, marking the second stage of casing treatment development. Takata and Tsukuda [7] performed an experimental study on a low-speed compressor. They noticed that the flow separation occurs on the suction side near the blade tip when the blade loading is increased. With casing treatment, the flow in the rear of the slot will be pushed into the slot and injected into the main flow as a jet at the forepart, which will result in a momentum transform between the moving wall and the low energy flow on the blade boundary layer. Smith and Cumpsty [8] measured flow patterns in detail, using hot wire anemometry, high response transducers, and a rotating probe. The stability enhancement mechanism they pointed out is the extraction of the low momentum fluid from the blade pressure side. Typically, for most slot-type casing treatments, the low energy fluid causing blockage in the passage will be pumped out and in turn, injected into the blade passage, driven by the pressure difference between two ends of the slot.

In the third stage, more efforts are now focused on the effect of casing treatments on the tip clearance flow, which plays a significant role in compressor stall onset [9–12]. With increasing blade loading, the tip leakage vortex moves upstream and blocks the blade passage. The vortex core may become unstable or broken when it passes through the shock in transonic compressors [13], or suffers a high adverse pressure gradient in subsonic compressors [14]. Based on the numerical results, Sakuma et al. [13] concluded that the stall delay mechanism is the reduction in the leakage flow momentum. Muller et al. [15] found that the rolling-up of the tip leakage vortex is suppressed and the blockage in blade passage is decreased when a circumferential groove casing is applied. According to their analysis, this is because on the one hand, the blade loading is reduced by the groove and on another, the tip leakage vortex is restricted near the suction side of the blade by the flow in and out of the groove. Houghton and Day [16] experimentally and numerically investigated a casing groove at different positions over the rotor tip. They explained that the reason the casing treatment improves the stability of the compressor is that the early evolution of the tip leakage vortex is limited by the groove. Recently, results regarding a transonic compressor have shown that the casing treatment located at different positions over the rotor blade tip imposes different effect on the tip leakage vortex [17]. In Hah's work, he pointed out that the working mechanism of the casing treatment suppresses the tip leakage vortex [18].

We see that significant progress has been made on the mechanism of casing treatments. However, a recent trend in the aircraft engine is toward higher efficiency, greater thrust-to-weight ratio, lighter weight, and less noise emission. Thus, more attention should be focused on both compressor noise and stability.

Sun et al. [19,20] proposed using an unsteady casing treatment to suppress the stall related disturbances rather than modifying the flow condition near the rotor tip. In their theory, the casing treatment is a kind of impedance boundary that affects the origination and evolution of the stall precursors. On the other hand, in terms of fan/compressor noise control, many methods are reported and applied, such the use of a clocking stator, an acoustic liner, or a swept rotor [21–23]. The stall precursor wave and the sound wave are both small disturbances waves; therefore, it is theoretically possible to control both waves simultaneously. This idea motivated the present work.

In this paper, we propose a type of foam metal casing treatment. We will show that the casing treatment can enhance the stability and reduce the noise level of the compressor. This paper is structured as follows: In Section 2, the experimental model is introduced, including the test compressor, pressure transducers, and the structure of the casing treatment. In Section 3, compressor performances, with and without the casing treatment, are compared. The stall process, stall inception, and tip flow patterns are also analyzed and discussed. In Section 4, the main conclusions are summarized.

2. Experimental Approach

2.1. Axial Compressor TA36

The experimental investigation is carried out on a single-stage axial flow compressor TA36. A schematic view of the TA36 is shown in Figure 1. It is an open-loop structure with a bell mouth inlet and an annular throttle valve. The ambient air is sucked in through an inlet bell mouth, passes through the stage, and leaves the compressor through a throttle. The main design parameters are listed in Table 1. The compressor is driven by a serve motor, and the maximum operating speed is 3000 rpm. For a fixed speed line, compressor performance can be obtained from the choke point to the stall point by controlling the throttle valve. All tests in this paper were performed at the design speed, which enables the Reynolds number to be greater than 1.0×10^5, based on the blade chord.

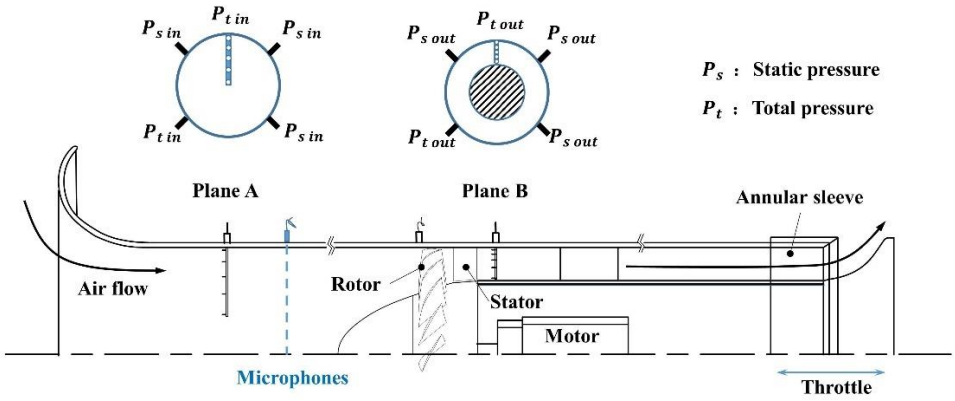

Figure 1. Schematic of the axial compressor.

Table 1. Design parameters for the compressor.

	Rotor	Stator
Blade number	20	27
Tip stagger angle (°)	60	7
Tip radius (mm)	300	300
Aspect ratio	1.18	1.40
Inlet hub-to-tip ratio	0.577	0.669
Mid-span solidity	1.51	1.24
Tip clearance (mm)	0.7	0.5
Design flow coefficient φ_d	0.24	
Design pressure rise coefficient ψ_d	0.48	
Efficiency at the design point	88%	
Design operating speed (rpm)	2930	
Rotor tip axial chord (mm) C_{ax}	50	

2.2. Experimental Methods

The compressor performance characteristics are determined by static pressure and total pressure at the inlet and outlet of the compressor. Pressure signals from four taps circumferentially equispaced at the straight section (Plane A in Figure 1) of the inlet bell mouth are recorded and averaged to calculate the axial flow velocity. The axial flow velocity is further normalized by the rotor rotation speed at mid-span U_m, denoted as the flow coefficient φ:

$$\varphi = \frac{V_x}{U_m} \tag{1}$$

At the section (Plane B in Figure 1) downstream of compressor stage, pressure signals from four equally-spaced taps are obtained and averaged to calculate the pressure rise $\Delta p = p_{s,out} - p_{t,in}$, where the $p_{s,out}$ is the average static pressure at Plane B, and the $p_{t,in}$ is the total pressure in inlet. The pressure rise coefficient is calculated by

$$\psi = \frac{\Delta p}{0.5\rho U_m^2} \tag{2}$$

The compressor efficiency is calculated using the shaft torque

$$\eta = \frac{Q(p_{t,out} - p_{t,in})}{\omega\tau} \tag{3}$$

where Q is the volume flow rate, ω is the rotational speed, τ is the torque, and $p_{t,out}$ is the total pressures at the outlet.

The unsteady casing wall pressure signals are measured using high-response transducers. The layout of the pressure transducers is given in Figure 2. Eight transducers are

evenly flush-mounted along the circumference of the annular, at 0.4 C_{ax} upstream of the rotor leading edge. Another eight transducers are installed on the casing wall covering the measure points from 9 mm upstream of the rotor leading edge to 7 mm axially downstream of the rotor trailing edge. The sampling frequency is set as 50 kHz, resulting in about 51 measuring points per blade passage.

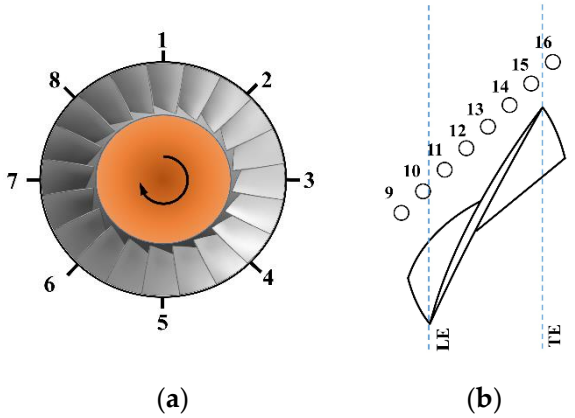

(**a**) (**b**)

Figure 2. Layout of the pressure transducers: (**a**) circumferential distributed transducers, (**b**) chord distributed transducers.

The compressor in-duct acoustic level is evaluated using sixteen evenly-spaced microphones (G.R.A.S. 40BH) located at about one diameter upstream of the rotor leading edge. Each data recording is performed at a fixed operation point in which the compressor has been operating stably for a period of time. All microphones are mounted flush on the casing wall. It should be noted that the final *SPL* is calculated with an energy-averaged acoustic pressure $\overline{p}$ of sixteen sets of signals. The uncertainty of the *SPL* is about 0.13 dB.

2.3. Foam Metal Casing Treatment

The casing treatment used in the present experiment is a type of foam metal casing treatment (FMCT). The foam metal resembles a sponge metal material, with plenty of small interlinked cavities. It allows airflow to move through it, but with some resistances. Our original intention when proposing FMCT was to try to create an impedance boundary condition which affects the birth and evolution of small disturbances (such as stall precursors).

In this paper, the open-cell foam metal is used. The foam metal has a porosity of 96%, and its PPI (pores per inch) is 35. We designed a foam metal ring embedded in the casing, as shown in Figure 3. Figure 3a is a photograph of the FMCT. Figure 3b presents a side schematic view of the FMCT. The foam metal ring has an axial length of 25 mm and a radial thickness of 20 mm. The front face of the foam metal ring is at 5 mm upstream of the rotor leading edge. Figure 3c provides a top view. It is shown that the foam metal ring covers 40% of rotor tip chord axially.

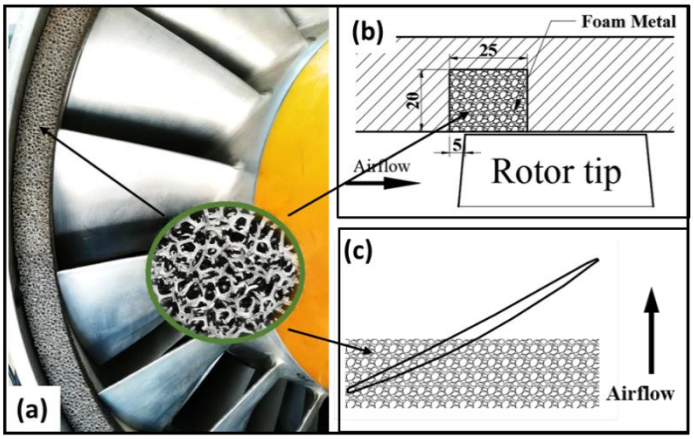

Figure 3. Configuration of the FMCT. (**a**) photograph of the FMCT, (**b**) side schematic view, (**c**) top schematic view.

3. Results and Discussion

3.1. Compressor Performance Characteristics

(a) Compressor performance characteristics

Figure 4 shows the compressor characteristics, with and without casing treatment. For brevity, the FMCT is abbreviated as CT, and the SC refers to the smooth casing wall condition. The stall point defined in this paper is the last stable operation point of the compressor at a fixed speed line. In Figure 4, the ordinate in the left vertical axis is the pressure rise coefficient, while the one on the right is the efficiency coefficient. The abscissa is the flow coefficient. Among the four curves, the circle refers to the pressure rise characteristic, and the diamonds denote the efficiency characteristic. In addition, the curve using open symbols refers to CT, and the solid symbols refer to SC. Comparing the pressure rise characteristics, we see that with CT, the compressor forms an extension of the curve for SC. The calculated SMI (stall margin improvement) is 14.9%. Regarding efficiency characteristic, the two curves nearly coincide with each other, which means that the CT results in nearly no efficiency loss.

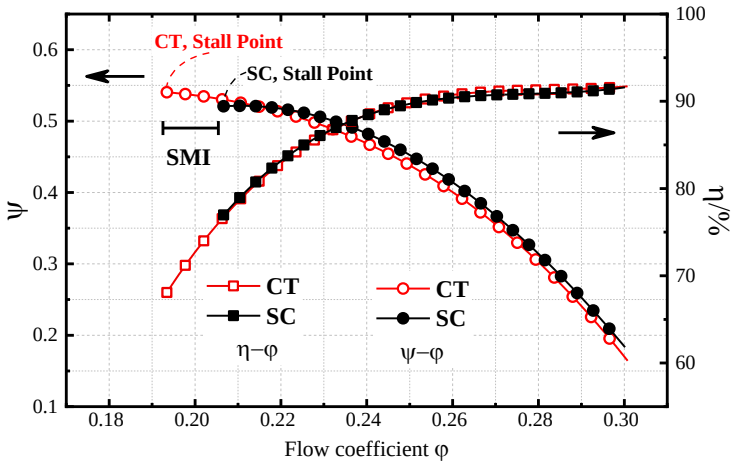

Figure 4. Compressor performance characteristics: pressure rise characteristic (**left**); efficiency characteristic (**right**).

(b) Noise characteristics

Figure 5 presents the noise frequency spectrum obtained at the design point of the compressor. The black line and the red line refer to SC and CT, respectively. The ordinate is *SPL* (sound pressure level) and the abscissa is frequency. The dominant sound source of

TA36 is the interaction noise at the third order BPF (blade passing frequency), as shown in Figure 5. It appears that, especially at the third BPF, the tonal noise is reduced by 3.2 dB in the CT condition.

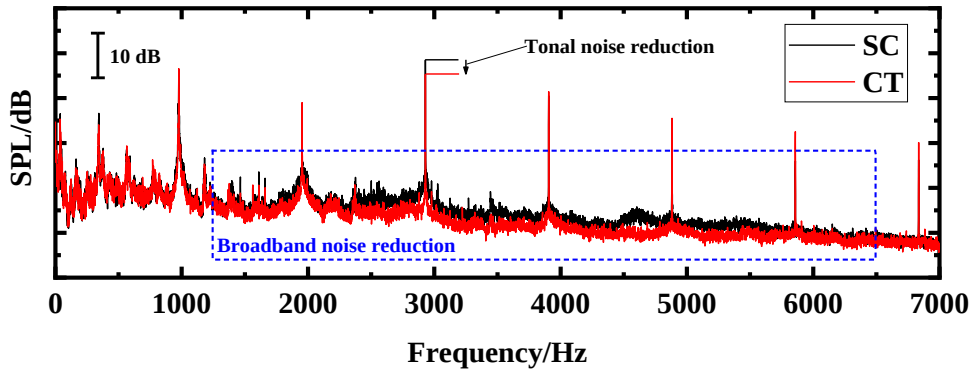

Figure 5. Noise spectrum of the compressor, with and without CT at DP.

As indicated by a blue dashed box, the broadband noise level of the compressor is also reduced in the CT condition. To make a more quantitative comparison regarding broadband noise, the energy-averaged *IL* (insertion loss) is calculated at each BPF band. The procedure is as follows: the first step is removing the tonal noise at each order of BPF. The next step is to divide the noise spectrum into several harmonic bands centered on each order of BPF. In the third step, the sound energy in each band is averaged into one representative *SPL*. At last, the *IL* is obtained by

$$IL = SPL_{SC} - SPL_{CT} \tag{4}$$

Figure 6 shows the *IL* in the first six orders of the harmonic bands. It is found that the *IL* is distributed between 1.5 and 2.4 dB. The maximum *IL* appears at the third and fourth order bands.

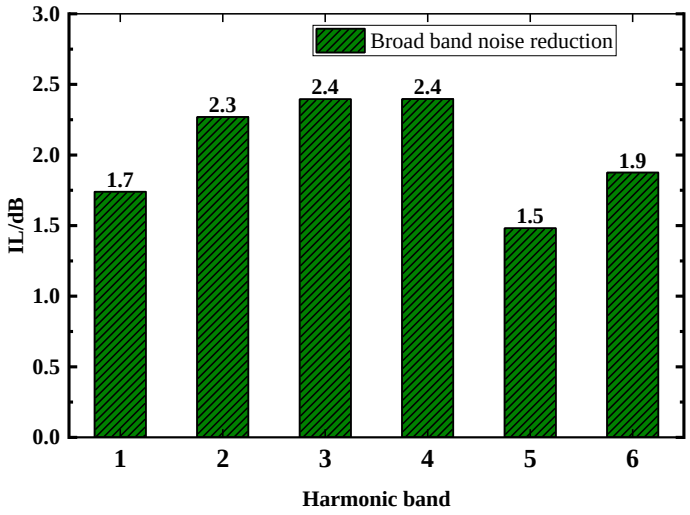

Figure 6. *IL* of CT at the first six harmonic bands.

Looking back at Figure 5, it is found that in the CT condition, both tonal noise (especially at the third order of BPF, which is the dominant noise source) and broadband noise are attenuated. The tonal noise in the compressor comes mainly from the interaction between the potential fields around the blades or the wake that interacts with the downstream stator blade. In the present experiment, the CT is only installed over the rotor tip rather than over the stator, so the reason for reducing the tonal noise may not be

that it suppresses the pressure fluctuation on the stator surface. It is supposed that the CT affects the wake or some other secondary flows due to the permeable feature of the foam metal. In addition, the broadband noise is also reduced in the CT condition, as shown in Figures 5 and 6. This is partly because the acoustic absorption, through the viscous and thermal dissipation, occurs inside the foam metal.

The above results are aimed at investigating the effect of the CT at the design point. However, the compressor may not always work at the design point. Therefore, it is necessary to test the CT under off-design conditions. For this purpose, acoustic levels at different mass flow points during the throttling process are measured and compared.

Figure 7 displays the curves of OASPL (overall sound pressure level) versus the mass flow, where the bandwidth of the calculation is from 20 Hz to 16,384 Hz. In Figure 7, the black symbols refer to the SC, and the red symbols refer to the CT. A marked difference in the OASPL curves for SC and CT can be noted. First of all, near the choke point, the OASPL in CT is a little higher than that in SC. However, at the other smaller mass flow points, the OASPL is reduced in the CT. For both casing conditions, the OASPL is at the lower value when the compressor operates near the design point (6.5 kg/s). The reason for the lower OASPL is that the stage is well matched at this point. The OASPL is increasing with the compressor throttling to the near stall point. This is because the blade loading increases during this process, which results in a higher pressure change along the blade. In summary, in the present experiment, the OASPL reduction generated by the CT is up to 3.1 dB during the throttling process, except the near choke point. It should be noted that a microphone is subjected to fluctuations, both in the sound and the pseudo-sound, when a measurement is performed in the near field. The compressor noise, therefore, contains the contribution of the pseudo-sound. A far-field acoustic experiment is under consideration to exclude the interference of pseudo-sound.

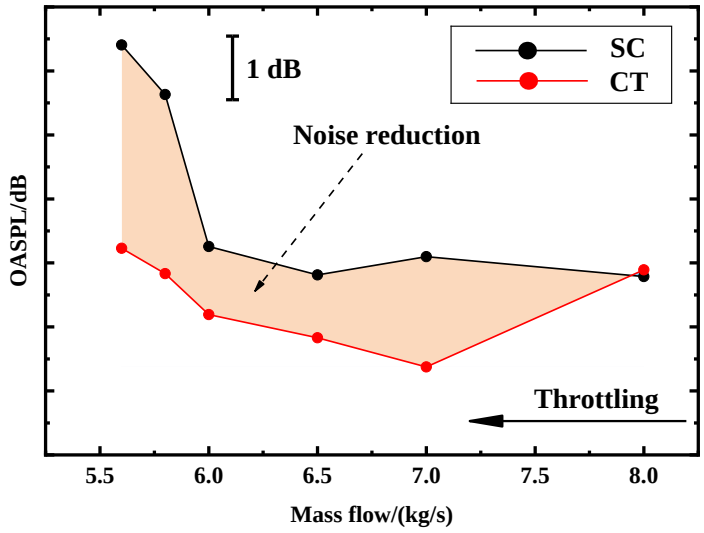

Figure 7. OASPL of the compressor, with and without CT, during the throttling process.

3.2. Stall Process Analysis

In Section 3.1, a comparison of the performance characteristics indicates that the CT improves the stall margin and reduces the noise level of the compressor. To further understand the work mechanism, the stall processes and the rotor tip flow field of the compressor, with and without the CT, are measured and analyzed in the following sections.

Figure 8 shows the stall process of the compressor in the SC. There are eight wall pressure signal traces. The pressure measurements are obtained by eight high-response transducers mounted upstream of the rotor leading edge, as introduced in Section 2.2. The abscissa is time represented by the period of a rotor revolution (the start point is set arbitrarily). The ordinates are normalized wall pressures, respectively. The raw data are

bandpass filtered from 2 to 500 Hz. As circled by a red oval, the "spike" appears with a sudden pressure rise, followed by a rapid drop. Once it emerges, this pattern grows in both length and strength as it travels along the circumferential annulus of compressor. After several revolutions, the spike develops into rotating stall cells, as shown in Figure 8. These data suggest that the compressor is a "spike-type" stall onset in the SC.

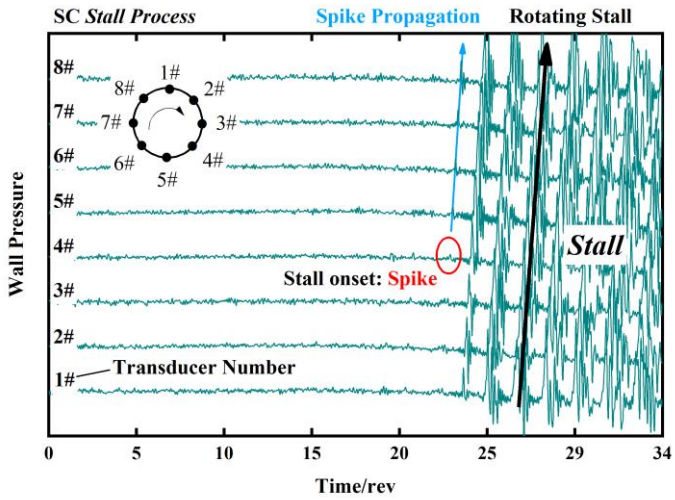

Figure 8. Eight wall pressure traces during the throttling of the compressor in SC.

Figure 9 shows the stall process of the compressor with CT. It can be seen that in the CT condition, the compressor also stalls via a spike-type stall onset. In addition, the FFT transform is performed on a single set of transducer measurement data during the stall process of the compressor in SC and CT, respectively. The frequency spectrum for the SC and the CT are shown in Figure 10. One can see that the travelling frequency of the stall cell is about half that of the compressor rotor frequency in either the SC or CT condition. This indicates that the CT dose not change the travelling speed of the developed rotating stall cell.

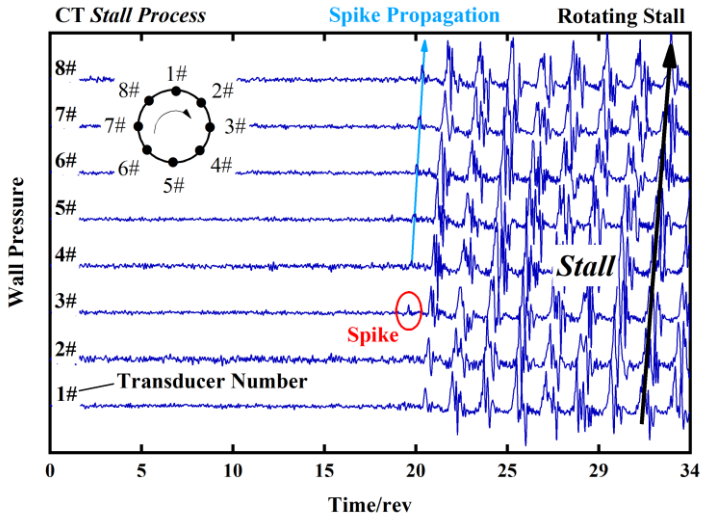

Figure 9. Eight wall pressure traces during throttling to stall the compressor in CT.

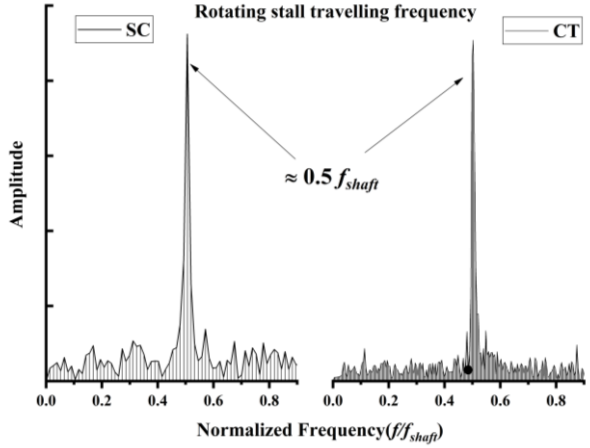

Figure 10. Frequency spectrum of the compressor during the stall process, with and without CT.

3.3. Prestall Disturbances Analysis

In this section, further attention is placed on the pre-stall stage. It is known that stall precursors are active before the rotating stall occurs. In fact, many flow disturbances appear in the stall process; those which actually trigger the compressor stall are called stall precursors. The key to the active control technology used to improve the stall margin of the compressor is to cancel the stall precursors. We also believe that the energy of the precursors can be suppressed by the CT. As opposed to the solid casings, the foam metal creates a "soft" wall condition for the precursor waves. When these waves are incident in foam metal surface, part of the wave will penetrate into the foam metal and be dissipated. Based on the understanding above, we can compare the energy level of the flow disturbances at the same operating point of the compressor in both SC and CT.

As He [24] has pointed out, the most unstable mode of disturbance is generally concentrated in the lower order. In the present experiment, the first mode of flow disturbances is investigated. The modal information can be obtained by performing the spatial Fourier decomposition of the data measured by the eight transducers, as presented in Section 3.2. The calculated Fourier coefficient is a complex number containing information on the spatial position and amplitude of the propagating disturbances. As shown in Equation (5), we refer the Fourier coefficient as C_k. C_k is a function of time and the mode k.

$$C_k(t) = \frac{1}{N}\sum_{n=0}^{N-1} P_n(t)\exp\left[-\frac{2kn\pi i}{N}\right] \tag{5}$$

In Equation (5), $P_n(t)$ is the pressure measurements from the n-th transducer of N high-response transducers. N is 8 in the present experiment.

In addition, the power spectrum density (PSD) is calculated based on the FFT on C_k. To be specific, $F(\omega)$ is the FFT coefficient of C_k, and the PSD is calculated from

$$PSD = \frac{|F(\omega)|^2}{M} \tag{6}$$

where M is the total number of the data points. More detail can be found in Ref. [25].

Figure 11 presents the amplitude of C_1 evolving over time. The black line refers to the SC condition, while the red line corresponds to the CT condition. As marked by a blue box, the flow disturbances are active, since the amplitude is not zero. When the compressor is throttling to a small mass flow point, in SC, the amplitude of disturbance is increased rapidly, which means that the rotating stall occurs. However, in CT, the disturbance amplitude remains at the same low level as before.

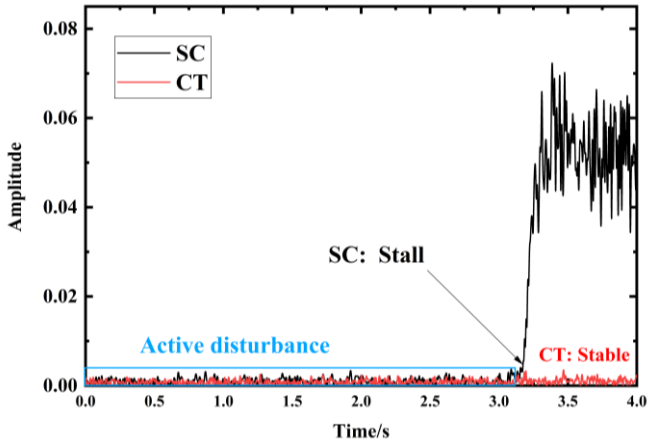

Figure 11. Development of C_1 amplitude in SC and CT when the compressor is slowly throttling to the stall point.

In the frequency domain, the disturbance energy is calculated and compared. Two sets of 100 revolutions-long data before the stall point of the compressor in the SC are measured; one is obtained in the SC condition, and the other is obtained in the CT condition. In Figure 12, the left graph shows the *PSD* spectrum in the SC, and the right graph shows that in the CT. Two things are obvious: first, the peak value of *PSD* is decreased in CT. Second, the disturbance energy in the wide band range is also reduced. It is suggested that, in the CT condition, disturbances in a wide range of frequency bands are suppressed. As a result, the development of the disturbances (including stall precursors) is restricted. This is the reason why the stall is delayed.

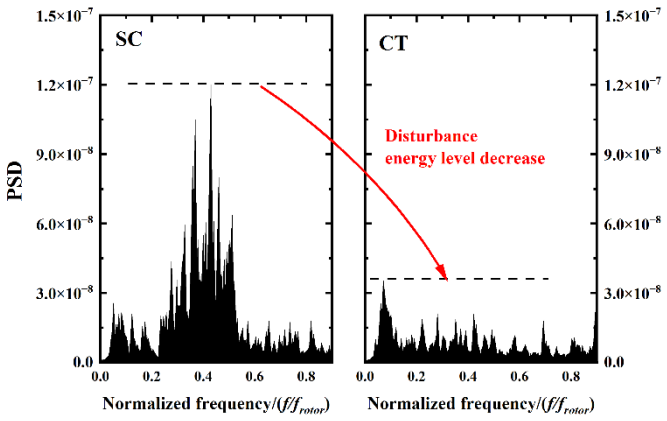

Figure 12. Comparison in *PSD* spectrum of C_1 in SC and CT.

3.4. Rotor Tip Flow Field

Tip clearance flow plays an important role in compressor stability, especially for the compressor that stalls via the spike-type stall inception. Vo et al. [10] proposed two necessary conditions related to tip clearance flow for the formation of spike disturbances: one is that the interface of the tip leakage flow and the incoming main flow become parallel to the inlet plane of the rotor at the LE (leading edge). The second is that a backflow of fluid in the adjacent passage occurs at the TE (trailing edge). Tip leakage flow is a flow structure through the blade tip clearance driven by the pressure difference between the pressure and suction sides of the blades. A tip leakage vortex (TLV) formed when the shear of the tip leakage flow and the incoming flow occurs. With increasing blade loading, the trajectory of TLV, as well as the interface of the tip leakage flow and the incoming flow, moves upstream.

With a goal to investigate the stall margin improvement mechanism of CT, in this section, the flow structures of the rotor tip region in SC and CT are analyzed. Figure 13

shows the phase-locked wall pressure contours of the compressor at DP (the design point in SC). C_p is the normalized wall pressure defined as

$$C_p = \frac{p_{wall} - p_0}{0.5\rho U_m^2} \tag{7}$$

where the p_{wall} is the measured wall pressure when the compressor is operating, and the p_0 is the wall pressure obtained when the compressor is not operating.

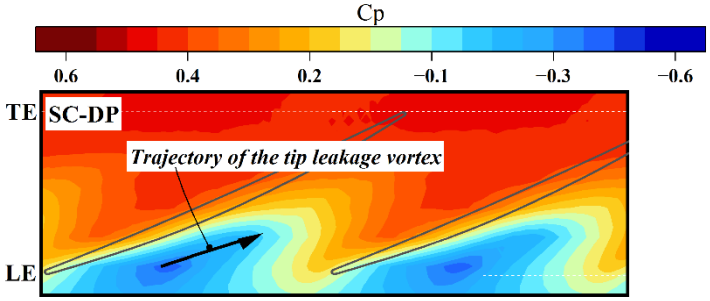

Figure 13. Tip flow structures of the compressor at DP.

In Figure 13, the position of LE and TE for the rotor blade, respectively, are shown by white dashed lines. The trajectory of the TLV is marked by a black arrow. It is seen that the TLV is formed on the suction side of the blade near the LE and is developed downstream of the passage.

The root-mean-square (*RMS*) of C_p, used as an indicator of the flow unsteadiness, is calculated by

$$RMS\ C_p = \sqrt{\frac{\sum_{i=1}^{N} \left(C_p(i) - \overline{C}_p\right)^2}{N}} \tag{8}$$

where N is the number of revolutions. The $C_p(i)$ is the non-dimensional pressure at the i-th revolution, and $\overline{C}_p$ is the average of $C_p(i)$ s in N revolutions.

Figure 14 shows the *RMS* C_p contour of the compressor at DP in the SC condition. As circled by a blue oval, the highest *RMS* C_p concentrates near LE on the suction side of blade tip. This is the region where the tip leakage flow and the incoming flow meet. The interaction of these two flows in different directions results in a strong pressure fluctuation. Another high *RMS* region, indicated by a blue dashed line, refers to the interface of the tip leakage flow and the incoming flow.

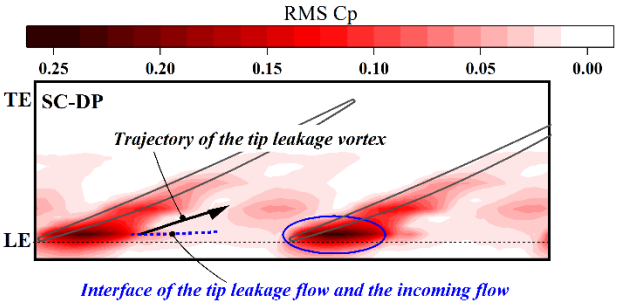

Figure 14. *RMS* C_p contours of the compressor at DP.

A comparison between the flow structures of the compressor at DP, with and without CT, is shown in Figure 15. In Figure 15c,d, the region covered by foam metal is marked by a green box and labeled as FM. One can see in Figure 15c that the minimum pressure area is near the trailing edge of the foam metal ring. However, in SC, the area is located near the

LE of the blade. The minimum pressure region is thought of as the origination of the TLV. It is suggested that in CT, the TLV is rolling up at the further downstream position of the passage compared with that in the SC. In addition, differences can be seen in the trajectory of the TLV for the two conditions such that the TLV tends to occur at the adjacent blade in the CT.

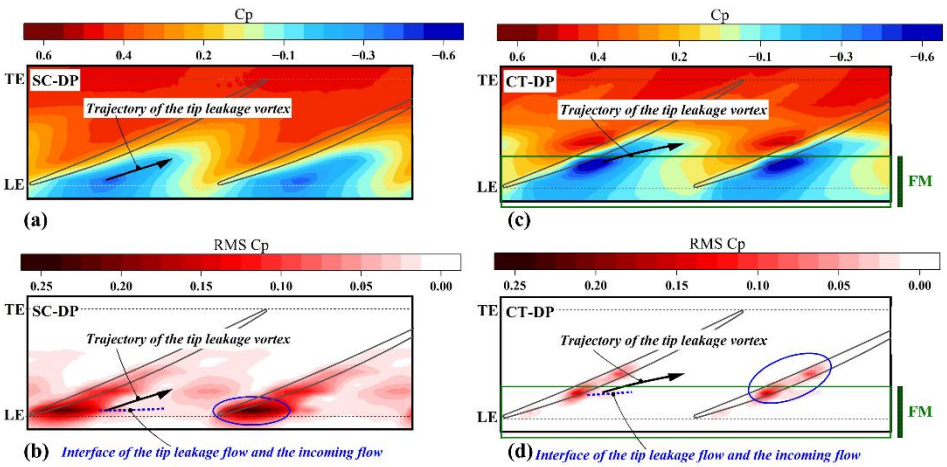

Figure 15. Comparison of tip flow structure of the compressor, with and without casing treatment, at DP. (**a**) C_p contours with SC, (**b**) RMS C_p contours with SC, (**c**) C_p contours with CT, (**d**) RMS C_p contours with CT.

Figure 15d shows the *RMS* C_p contours in the CT. There are three features that should be considered. First, the highest *RMS* region near the LE, as circled in Figure 15b, disappears in the CT condition. The second difference is that the highest *RMS* region appears near the trailing edge of the foam metal ring where the TLV is formed. Third, as indicated by a blue dashed line, the interface of the tip leakage flow and the incoming flow is also located further downstream, compared with that in the SC.

The flow structures in SC and CT when the compressor is throttled into NSP (the near stall point in SC) are show in Figure 16. In SC, it is seen that the TLV is still in the blade passage. The interface of the tip leakage flow and the incoming flow is nearly parallel to the LE plane of the rotor. The notable change is that the *RMS* level near the LE is increased. This can be understood if one remembers that the strength of the tip leakage is increasing with the throttling process, since the blade loading is increasing at the same time. In CT, as marked by a black arrow, the trajectory of the TLV is more circumferential, but it is still located near the trailing edge of the foam metal ring. It is shown in Figure 16d that the highest *RMS* region is still concentrated near the corner of the suction side of the blade and the trailing edge of the foam metal ring.

These comparisons made between the flow structures of the compressor in SC and CT suggest that the CT affects the behavior of the tip clearance. First of all, the origination point of the TLV is moved to the downstream position of the passage in CT. In the regions covered by the foam metal, the tip leakage flow is weak, hence the rolling-up of the TLV is unsustainable. Since the strength of the tip leakage flow is determined by the local blade loading, it is thus deduced that the blade loading is reduced in this region. This conclusion can also be confirmed if one can compares the pressure contours covered by the foam metal in Figure 15a,c or Figure 16a,c. On the other hand, at NSP, the interface of the tip leakage flow and the incoming flow is nearly parallel to the LE of rotor. However in CT, the interface is located downstream.

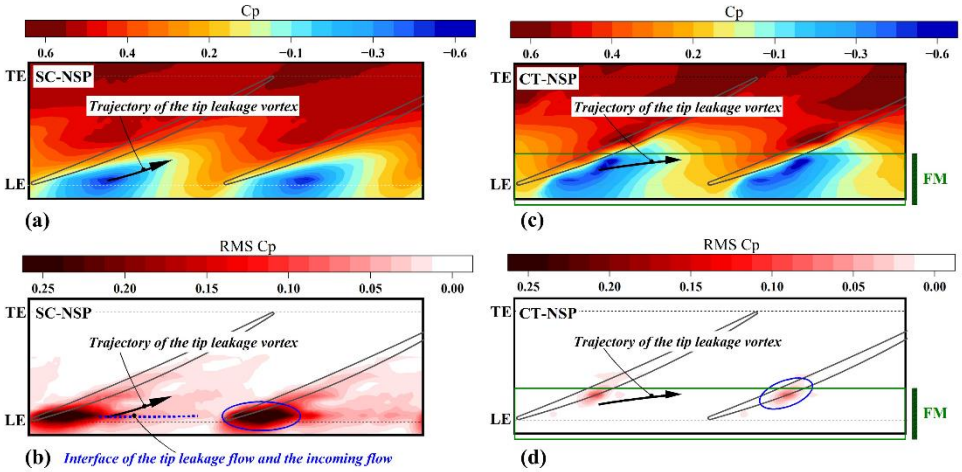

Figure 16. Comparison of tip flow structure of the compressor, with and without casing treatment, at NSP. (**a**) C_p contours with SC, (**b**) RMS C_p contours with SC, (**c**) C_p contours with CT, (**d**) RMS C_p contours with CT.

To further understand the behavior of the TLV in CT, the flow structure of the compressor at NSPCT (the near stall point in CT) is plotted in Figure 17. The scale of the *RMS* contours is adjusted to provide more information. When the compressor is throttling from DP to NSPCT, it is shown in Figure 17a–c that the position of the minimum pressure region is moved upstream from the trailing edge of the foam metal ring to the place near the LE of the rotor. It is noted that for the compressor in the SC, the peak loading position on the rotor blades moves to the leading edge during the throttling process [26]. In the CT, because the blade loading is reduced in the region near the LE of the rotor blade, at NSP, the region of the maximum blade loading is located near the trailing edge of the foam metal ring.

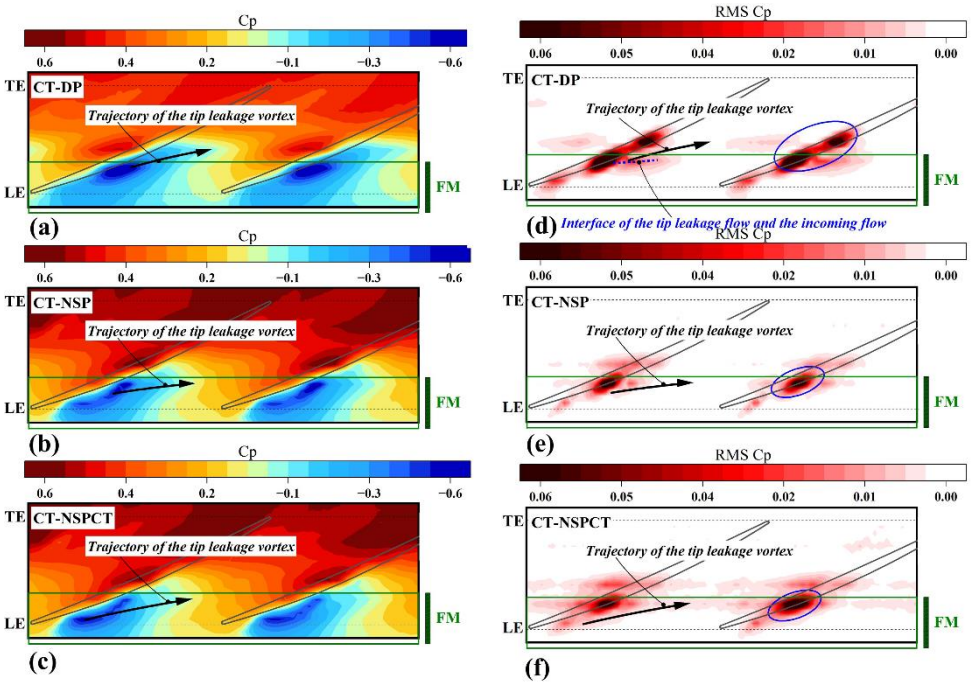

Figure 17. Evolution of the tip flow structure of the compressor with casing treatment. (**a**) C_p contours at DP, (**b**) C_p contours at NSP, (**c**) C_p contours at NSPCT, (**d**) RMS C_p contours at DP, (**e**) RMS C_p contours at NSP, (**f**) RMS C_p contours at NSPCT.

In Figure 17d–f, one can see that at DP, there are two higher *RMS* regions on both sides of the trailing edge of the foam metal ring. At NSP, there is only one highest *RMS*

region located in the corner of the blade suction side and the trailing edge of the foam metal ring. To further throttle the compressor to the NSPCT, the highest *RMS* region dose not moved upstream. It is thus deduced that in the CT, the origination and the evolution of the TLV are influenced by the foam metal. In the CT, the TLV is formed at a position further downstream, and its trajectory tends to be circumferential, but is still located in the blade passage when the compressor is operating at NSP.

3.5. Frequency Spectrum Analysis

The analysis on the tip flow structure is further performed in the frequency domain, as shown in Figure 18. The three operating points regarding the characteristics are presented in Figure 18f. The three graphs in the upper part of the Figure 18 are related to the CT, and the lower two graphs are corresponding to the SC. In each graph, the ordinate is the frequency normalized by the rotor frequency. The frequency at ordinate 20 is the BPF. The abscissa is the spatial location of the transducers, and the positions of the LE and the TE are marked by white lines, respectively. At DP, in the SC, the peak at BPF corresponds to a disturbance associated with a slight rotor asymmetry. While in the CT, in the region from LE to about 50% of the blade chord, the peak at BPF may be related to the pressure fluctuation caused by the in and out flow from the foam metal. At NSP, we can see in Figure 18e that a frequency band concentrates near the LE of the rotor. This is because the interface of the tip leakage flow and the incoming flow is nearly parallel to the LE in this region. The interaction of these two flows results in a strong pressure fluctuation. However, in Figure 18b, a band from 15% to 50% of the blade chord is dominant. This is because the TLV is formed in this region, as shown in Figure 17e. When the compressor is throttling to NSPCT, the peak frequency is in the band from 15% to 50% of the blade chord, but the strength of the fluctuation is increased. This phenomenon coincides with the results in Figure 17f.

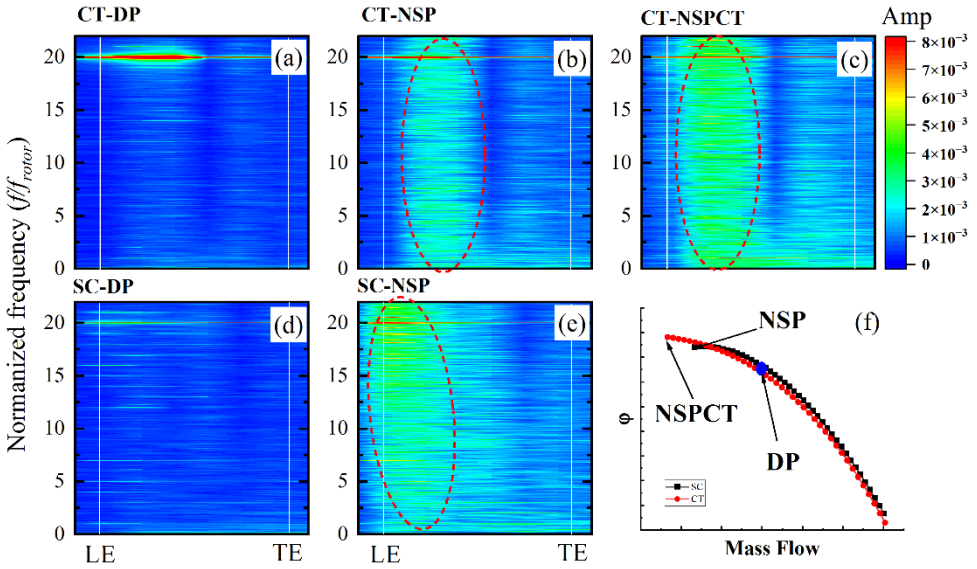

Figure 18. Comparison of frequency spectrum of the compressor, with and without casing treatment. (**a**) frequency spectrum with CT, at DP, (**b**) frequency spectrum with CT, at NSP, (**c**) frequency spectrum with CT, at NSPCT, (**d**) frequency spectrum with SC, at DP, (**e**) frequency spectrum with SC, at NSP, (**f**) pressure rise characteristics of the compressor.

4. Conclusions

In this paper, we focus on the stall margin improvement and noise reduction of a compressor. A casing treatment based on foam metal is proposed and tested. Both steady performance characteristic and the stall process of a compressor, with and without casing treatment, are compared and analyzed. The main conclusions are summarized as follows:

In the present experiment, the CT can improve the stall margin by 14.9% without efficiency loss. In addition, this CT is effective in increasing the flow range and pressure rise of the compressor.

When the CT is applied, the acoustic level of the compressor is reduced. The test compressor is a "tonal-dominant" machine, and the noise peak point appears at the third order of BPF. At this point, the tonal noise *SPL* is reduced by 3.2 dB in the CT condition. The calculated insertion loss shows that the *SPL* of the broadband noise can be reduced up to 2.4 dB. Furthermore, the OASPL reduction is up to 3.1 dB during the throttling process.

The CT affects the behavior of the TLV. In the SC, the TLV is formed in the suction side and near the leading edge of the rotor blade, since the CT reduces the blade loading near the leading edge of the rotor blade. In the CT, the TLV is appears in the region at about 40% of the blade chord downstream from the leading edge. The trajectory of the TLV tends to be circumferential, but is still located in the blade passage during the throttling process.

The stall suppression is thought to be due to the effect of the CT on the TLV, which originates from the region covered by the foam metal. The attenuation in the tip leakage flow causes a delay regarding all stall precursors.

Author Contributions: Conceptualization, X.S. and D.S.; methodology, X.D. and J.L.; software, J.L.; validation, Y.W., C.G. and X.D.; formal analysis, J.L.; investigation, J.L.; resources, D.S.; data curation, D.S.; writing—original draft preparation, J.L.; writing—review and editing, D.S. and X.D.; visualization, Y.W. and C.G.; supervision, X.S.; project administration, X.S. and D.S.; funding acquisition, X.S. and D.S. All authors have read and agreed to the published version of the manuscript.

Funding: Funding for this study was provided by the National Natural Science Foundation of China (51790514), the National Science and Technology Major Project (2017-II-003-0015) and the Key Laboratory of Pre-Research Management Center (6142702200101).

Data Availability Statement: The data presented in this study are available on request from the corresponding author.

Conflicts of Interest: The authors declare no conflict of interest.

References

1. Koch, C.C.; Smith, L.H., Jr. *Experimental Evaluation of Outer Case Blowing or Bleeding of a Single Stage Axial Flow Compressor, Part II–Part VI*; NASA CR-54588-92; Lewis Research Center: Cleveland, OH, USA, 1966.
2. Hathaway, M.D. *Passive Endwall Treatments for Enhancing Stability*; U.S. Army Research Laboratory: Adelphi, MD, USA, 2007.
3. Bailey, E.E.; Voit, C.H. *Some Observations of Effects of Porous Casings on Operating Range of a Single Axial-Flow Compressor Rotor*; NASA TM X–2120; Lewis Research Center: Cleveland, OH, USA, 1970.
4. Osborn, W.M.; Lewis, G.W., Jr.; Heidelberg, L.J. *Effect of Several Porous Casing Treatments on Stall Limit and Overall Performance of an Axial-Flow Compressor Rotor*; NASA TN D–6537; Lewis Research Center: Cleveland, OH, USA, 1971.
5. Prince, D.C.; Wisler, D.D.; Hilvers, D.E. *Study of Casing Treatment Stall Margin Improvement Phenomena*; NASA CR–134552; General Electric Co.: Cincinnati, OH, USA, 1974.
6. Fujita, H.; Takata, H. A Study of Configurations of Casing Treatment for Axial Flow Compressors. *Bull. JSME* **1984**, *27*, 1675–1681. [CrossRef]
7. Takata, H.; Tsukuda, Y. Stall Margin Improvement by Casing Treatment—Its Mechanism and Effectiveness. *ASME J. Eng. Power* **1977**, *99*, 121–133. [CrossRef]
8. Smith, G.D.J.; Cumpsty, N.A. Flow Phenomena in Compressor Casing Treatment. *ASME J. Eng. Gas Turbines Power* **1984**, *106*, 532–541. [CrossRef]
9. Hoying, D.A.; Tan, C.S.; Vo, H.D.; Greitzer, E.M. Role of Blade Passage Flow Structures in Axial Compressor Rotating Stall Inception. *ASME J. Turbomach.* **1999**, *121*, 735–742. [CrossRef]
10. Vo, H.D.; Tan, C.S.; Greitzer, E.M. Criteria for Spike Initiated Rotating Stall. *J. Turbomach.* **2008**, *130*, 11023. [CrossRef]
11. Pullan, G.; Young, A.M.; Day, I.J.; Greitzer, E.M.; Spakovszky, Z.S. Origins and Structure of Spike-Type Rotating Stall. *J. Turbomach.* **2015**, *137*, 51007. [CrossRef]
12. Hewkin-Smith, M.; Pullan, G.; Grimshaw, S.D.; Greitzer, E.M.; Spakovszky, Z.S. The Role of Tip Leakage Flow in Spike-Type Rotating Stall Inception. *J. Turbomach.* **2019**, *141*, 61010. [CrossRef]
13. Sakuma, Y.; Watanabe, T.; Himeno, T.; Kato, D.; Murooka, T.; Shuto, Y. Numerical Analysis of Flow in a Transonic Compressor With a Single Circumferential Casing Groove: Influence of Groove Location and Depth on Flow Instability. *J. Turbomach.* **2013**, *136*, 31017. [CrossRef]

14. Furukawa, M.; Inoue, M.; Saiki, K.; Yamada, K. The Role of Tip Leakage Vortex Breakdown in Compressor Rotor Aerodynamics. *ASME J. Turbomach.* **1999**, *121*, 469–480. [CrossRef]
15. Muller, M.W.; Schiffer, H.-P.; Hah, C. Effect of Circumferential Grooves on the Aerodynamic Performance of an Axial Single-Stage Transonic Compressor. In Proceedings of the ASME Turbo Expo 2007: Power for Land, Sea and Air, Montreal, QC, Canada, 14–17 May 2007.
16. Houghton, T.; Day, I. Enhancing the Stability of Subsonic Compressors Using Casing Grooves. *J. Turbomach.* **2010**, *133*, 021007. [CrossRef]
17. Wu, X.; Liu, B.; Zhang, B.; Mao, X. Effect of circumferential single casing groove location on the flow stability under tip-clearance effect in a transonic axial flow compressor rotor. *Energies* **2021**, *14*, 6143. [CrossRef]
18. Hah, C. The Inner Workings of Axial Casing Grooves in a One and a Half Stage Axial Compressor with a Large Rotor Tip Gap: Changes in Stall Margin and Efficiency. *J. Turbomach.* **2018**, *141*, 11001. [CrossRef]
19. Sun, D.; Liu, X.; Jin, D.; Gui, X.; Sun, X. Theory of Compressor Stability Enhancement Using Novel Casing Treatment, Part II: Experiment. *J. Propuls. Power* **2014**, *30*, 1236–1247. [CrossRef]
20. Sun, X.; Sun, D.; Liu, X.; Yu, W.; Wang, X. Theory of Compressor Stability Enhancement Using Novel Casing Treatment, Part I: Methodology. *J. Propuls. Power* **2014**, *30*, 1224–1235. [CrossRef]
21. Milidonis, K.; Semlitsch, B.; Hynes, T. Effect of Clocking on Compressor Noise Generatio. *AIAA J.* **2018**, *56*, 4225–4231. [CrossRef]
22. Sutliff, D.; Jones, M. Low-Speed Fan Noise Attenuation from a Foam-Metal Liner. *AIAA J. Aircr.* **2009**, *46*, 1381–1394. [CrossRef]
23. Huff, D. Noise Reduction Technologies for Turbofan Engine. In Proceedings of the 35th International Congress and Exposition on Noise Control Engineering, NASA/TM—2007-214495. Honolulu, HI, USA, 3–6 December 2007.
24. He, L. Computational Study of Rotating Stall Inception in Axial Compressors. *J. Propuls. Power* **1997**, *13*, 31–38. [CrossRef]
25. Sun, D.; Nie, C.; Liu, X.; Lin, F.; Sun, X. Further Investigation on Transonic Compressor Stall Margin Enhancement with Stall Precursor-Suppressed Casing Treatment. *J. Turbomach.* **2015**, *138*, 21001. [CrossRef]
26. Xu, D.; Dong, X.; Zhou, C.; Sun, D.; Gui, X.; Sun, X. Effect of rotor axial blade loading distribution on compressor stability. *Aerosp. Sci. Technol.* **2022**, *127*, 107230. [CrossRef]